IEEE Access
Multidisciplinary | Rapid Review | Open Access Journal

Received April 26, 2021, accepted June 23, 2021, date of publication July 2, 2021, date of current version July 14, 2021.

Digital Object Identifier 10.1109/ACCESS.2021.3094409

A Low-Complexity Time-Domain Method for a Fast and Accurate Measurement of Q-Factor and Resonant Frequency of RF and Microwave Resonators

FATEMEH AKBAR, (Member, IEEE), BEHZAD YEKTAKHAH, (Member, IEEE), HAOKUI XU, (Graduate Student Member, IEEE), AND KAMAL SARABANDI, (Fellow, IEEE)
Radiation Laboratory, University of Michigan, Ann Arbor, MI 48109, USA

Corresponding author: Fatemeh Akbar (fatemeh@caltech.edu)

ABSTRACT A new time-domain technique for an accurate and fast measurement of the resonant frequency and Q-factor of resonators is presented. In this technique, the phase slope with respect to frequency of a resonator is characterized and used to specify its Q-factor and resonant frequency. To measure the phase slope, a slow-rate linear chirp signal is generated and passed through the resonator under test. The output signal is amplified and subsequently divided into two equal parts which are delayed by different amounts. Due to the linear time-frequency relationship of the chirp signal, the instantaneous frequencies of the two delayed signals are slightly different at any given time, and their phase difference can determine the resonator's phase slope. Detailed analysis of the proposed approach is presented and its accuracy is verified through simulations and measurements. Based on the measured results, the proposed approach characterizes the resonant frequency and Q-factor by less than 0.6% and 4% error, respectively.

INDEX TERMS Chirp signal, phase slope, Q-factor, resonant frequency, resonator, time-domain.

I. INTRODUCTION

Microwave resonators are one of the key components of communication, radar, and sensing systems. They have been broadly used in microwave filters, oscillators, and tuned amplifiers in communication and radar transceivers and have been largely utilized in sensors for different purposes such as material characterization [1]–[4], defect detection [5], chemical analysis [6], bio-sensing [7], qubit readout for quantum information processing [8], [9], motion control [10], and ambient monitoring [11]. There is also an emerging interest in microwave resonator-based sensors within the framework of the internet of things [12].

Microwave resonators can be employed particularly for characterizing complex dielectric constant of materials which helps with determining their certain aspects such as mass density or moisture content. This has been used in a variety of applications including geology (in particular, avalanche monitoring and agricultural planning), remote sensing, and underground survey using ground penetrating radar. The real and imaginary parts of the dielectric constant of a material can be determined, respectively, from the variations in resonant frequency and Q-factor of a resonator when it becomes in contact with the material under test. In general, it is important to characterize the resonant frequency and Q-factor of resonators accurately.

Several frequency and time-domain techniques for measuring the resonant frequency and Q-factor of resonators have been presented in the past. Frequency-domain techniques measure the resonator's transmission (or reflection) coefficient over a frequency range and detect the frequency of maximum transmission (or minimum reflection) in addition to the 3-dB bandwidth of the response. Such measurement techniques are precise but generally require costly and complex equipment such as vector network analyzers (VNA). On the other hand, typical time-domain approaches, which determine the Q-factor and resonant frequency of a resonator from its transient damped oscillatory response to an excitation [13], are low-cost and fast but less accurate. They also require high speed switches, comparators, and zero crossing detectors to characterize high-frequency resonators. A new, low-complexity, fast, and yet accurate time-domain approach to characterize the Q-factor and resonant frequency of second-order resonators was briefly introduced in [14]. In this approach, the derivative of insertion phase with respect to frequency (phase slope) of a resonator is determined and

The associate editor coordinating the review of this manuscript and approving it for publication was Mira Naftaly.

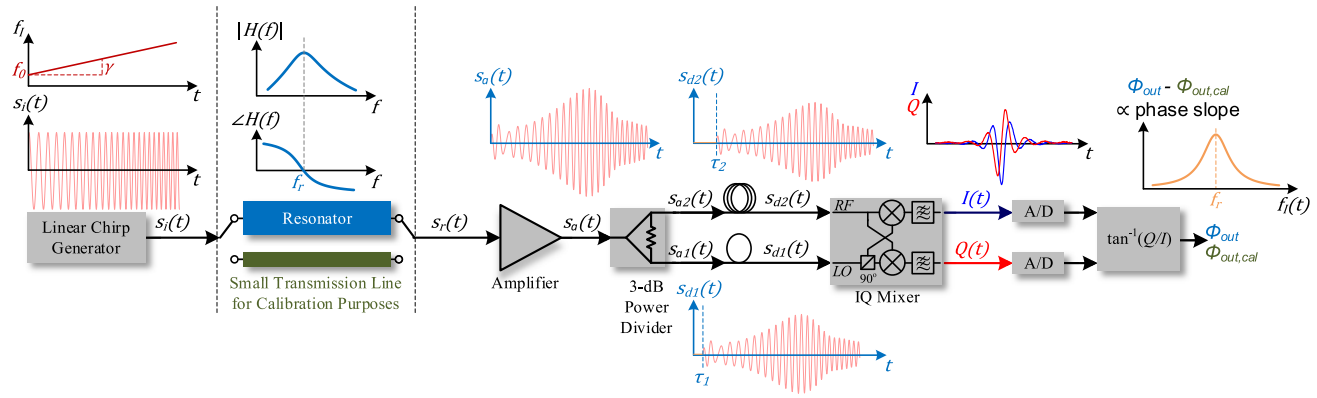

FIGURE 1. Block diagram of the proposed approach for characterizing the resonant frequency and *Q*-factor of resonators.

used to specify its *Q*-factor and resonant frequency. This paper extends [14] by *i*) elaborating on the operation principle of the new method, *ii*) analyzing its systematic error, and *iii*) providing some guidelines to enhance its accuracy. Furthermore, detailed simulation and measurement results, verifying the performance and accuracy of the introduced method, are presented.

In the proposed technique, a slow-rate linear chirp signal is generated and passed through the resonator under test. The resonator's output signal is divided into two equal parts which are subsequently delayed by two different time intervals. Due to the linear time-frequency relationship of the chirp, the two signals which are delayed by different time intervals have different instantaneous frequencies at any given time. The phase difference between these signals is measured and used to determine the resonator's phase slope and therewith its *Q*-factor and resonant frequency. This technique is realized using a low-complexity system and utilized for characterizing several L-band resonators. According to the measured results, it characterizes *Q*-factor and resonant frequency with less than 4% and 0.6% error, respectively.

II. RESONANT FREQUENCY AND Q-FACTOR MEASUREMENT APPROACH

In the frequency response of a second order resonator, the maximum value of absolute phase slope, $|d\phi/df|$, occurs at the resonant frequency (f_r) and is proportional to *Q*-factor following:

$$Q = \frac{f_r}{2}\left|\frac{d\phi\,(f)}{df}\right|_{f_r} = \frac{f_r}{2}\left(-\frac{d\phi\,(f)}{df}\right)\Big|_{f_r}. \tag{1}$$

As a result, the resonant frequency and *Q*-factor of a second-order resonator can be determined by measuring its phase slope within a frequency range including f_r. This is accomplished in this work by using a new linear time-invariant (LTI) measurement system shown in Fig. 1. The signal input to the resonator, $s_i\,(t)$, is a linear chirp [15], [16] with a duration of T and a complex representation of:

$$s_i\,(t) = e^{j\phi_0}e^{j2\pi\left(f_0+\frac{\gamma}{2}t\right)t}\,(u\,(t) - u(t-T))\,, \tag{2}$$

where f_0, γ, ϕ_0, t, and $u(t)$ denote the start frequency of the chirp, the chirp rate in Hz/s, the initial phase of the chirp, time, and the unit step function, respectively. The chirp instantaneous frequency, $f_I\,(t)$, is equal to $f_0 + \gamma t$. Assuming an impulse response of $h(t)$ for the resonator in Fig. 1 (or in general, any 2-port LTI system), its output in response to the chirp input is equal to:

$$s_r\,(t) = s_i\,(t) * h\,(t) = \int_{-\infty}^{+\infty} s_i\,(t-\tau)\,h\,(\tau)\,d\tau, \tag{3}$$

where $*$ denotes the convolution operation. For a second order resonator, $h(t)$ is zero for $t < 0$ (due to causality) and has a damping oscillatory form for $t > 0$. The value of $h(t)$ reduces to $1/k$ of its maximum at the time of $t_0(k) = Q\ln(k)\,/\,(\pi f_r)$ [13]. For a large value of k (e.g. 100), $h\,(t)$ is nearly zero at $t > t_0$. Assuming $t_0 \le T$, the integral in (3) can be written as:

$$s_r\,(t) = \begin{cases} \displaystyle\int_0^t e^{j\phi_0}e^{j2\pi f_0(t-\tau)}e^{j\pi\gamma(t-\tau)^2}h\,(\tau)\,d\tau & t < t_0 \\ \displaystyle\int_0^{t_0} e^{j\phi_0}e^{j2\pi f_0(t-\tau)}e^{j\pi\gamma(t-\tau)^2}h\,(\tau)\,d\tau & t > t_0. \end{cases} \tag{4}$$

For $t > t_0$, the lower and upper limits of the integral can be replaced by $-\infty$ and $+\infty$, respectively, (since $h\,(t)$ is zero for $t < 0$ and nearly zero for $t > t_0$) and $s_r(t)$ equals:

$$s_r\,(t)|_{t>t_0} = \int_{-\infty}^{+\infty} e^{j\phi_0}e^{j2\pi f_0(t-\tau)}e^{j\pi\gamma(t-\tau)^2}h\,(\tau)\,d\tau. \tag{5}$$

The resonator's output signal, $s_r(t)$, has transient temporal variations for $t < t_0$ and after the time t_0, it follows (5). Provided that the start frequency of the chirp signal is well below the resonant frequency of the resonator (such that $f_0 + \gamma t_0 < f_r$), $s_r(t)$ follows (5) when $f_I(t)$ is in the vicinity of f_r, which is the assumption made henceforth. Thus, $s_r(t)$ is given by:

$$\begin{aligned} s_r(t) &= \underbrace{e^{j\phi_0}e^{j2\pi f_0 t}e^{j\pi\gamma t^2}}_{s(t)} \int_{-\infty}^{+\infty} h\,(\tau)\,e^{j\pi\gamma\tau^2}e^{-j2\pi(f_0+\gamma t)\tau}\,d\tau \\ &= s\,(t) \times \mathcal{F}\left(h\,(\tau)\,e^{j\pi\gamma\tau^2}\right)\Big|_{f_0+\gamma t}, \end{aligned} \tag{6}$$

where $\mathcal{F}(.)|_f$ represents the Fourier transform of (.) at the frequency of f. Denoting the Fourier transform of $h(\tau)\, e^{j\pi\gamma\tau^2}$ by $H_s(f)$, we will have:

$$s_r(t) = s(t) \times H_s(f_I(t)), \tag{7}$$

where $f_I(t) = f_0 + \gamma t$. For a slow-rate chirp signal (a small value of γ) and/or a short duration for $h(t)$, corresponding to not a very high Q for the resonator, $H_s(f)$ is approximately equal to the resonator's transfer function, $H_r(f)$. Using this approximation, which is verified in Section III, (7) is nearly equal to:

$$s_r(t) \cong s(t) \times H_r(f_I(t)). \tag{8}$$

Considering that $s_r(t)$ is, in fact, a real signal, it is equal to:

$$\begin{aligned} s_r(t) &\cong \Re\left(e^{j\phi_0} e^{j2\pi\left(f_0+\frac{\gamma}{2}t\right)t} H_r(f_I(t))\right) \\ &\cong A_r(f_I(t)) \cos\left(2\pi\left(f_0+\frac{\gamma}{2}t\right)t + \phi_r(f_I(t)) + \phi_0\right), \end{aligned} \tag{9}$$

where A_r and ϕ_r are the amplitude and phase of H_r, respectively. $s_r(t)$ is amplified (to compensate for the insertion loss of the resonator) using an amplifier (Fig. 1) with a flat gain of A_v and a constant group delay of τ_g within the operation band. Subsequently, the amplified signal, $s_a(t)$, is divided by two (using a 3-dB power divider), generating $s_{a1}(t)$ and $s_{a2}(t)$ which are given by:

$$s_{a1}(t) = s_{a2}(t) = A_v \Big/ \sqrt{2}\, s_r(t - \tau_g - \tau_D), \tag{10}$$

where τ_D indicates the divider's delay. The signals $s_{a1}(t)$ and $s_{a2}(t)$ pass through a short and a longer coaxial cable with delays of τ_1 and τ_2, respectively. The delayed signals are given by:

$$s_{d1,2}(t) = G_{tot} s_r(t - \tau_{tot} - \tau_{1,2}), \tag{11}$$

where $G_{tot} = A_v \Big/ \sqrt{2}$ and τ_{tot} represents the total delay caused by the amplifier, the divider, and the interconnecting lines (which connect the blocks in Fig. 1). Substituting $s_r(t)$ from (9) in (11) results in:

$$\begin{aligned} &s_{d1,2}(t) \\ &\cong G_{tot} A_r\left(f_I\left(t-\tau_{tot}-\tau_{1,2}\right)\right) \\ &\quad \times cos\left(2\pi\left(f_0+\frac{\gamma}{2}\left(t-\tau_{tot}-\tau_{1,2}\right)\right)\left(t-\tau_{tot}-\tau_{1,2}\right)\right. \\ &\quad \left. + \phi_r\left(f_I\left(t-\tau_{tot}-\tau_{1,2}\right)\right) + \phi_0\right). \end{aligned} \tag{12}$$

The phase difference between s_{d1} and s_{d2} can determine the resonator's phase slope provided that the two instantaneous frequencies $f_I(t - \tau_{tot} - \tau_1)$ and $f_I(t - \tau_{tot} - \tau_2)$ are close enough (which is the assumption made henceforth). A phase detector block (here an I/Q mixer) in conjunction with analog to digital converters and a digital processing unit are used to measure the phase difference between s_{d1} and s_{d2} (ϕ_{out}) and subsequently determine the resonant frequency and Q-factor. This phase difference, ϕ_{out}, is given by:

$$\begin{aligned} \phi_{out}(t) \cong &\left(-2\pi\left(f_0+\gamma\left(t-\tau_{tot}\right)\right)+\pi\gamma\left(\tau_1+\tau_2\right)\right)\Delta\tau \\ &+ \underbrace{\left(\phi_r(f_I(t-\tau_{tot}-\tau_2)) - \phi_r(f_I(t-\tau_{tot}-\tau_1))\right)}_{\Delta\phi_r(t)}, \end{aligned} \tag{13}$$

where $\Delta\tau = \tau_2 - \tau_1$. The last term in (13), indicated by $\Delta\phi_r(t)$, is proportional to the resonator's phase slope which is the quantity of interest, while the other term is undesired. Knowing the system parameters f_0, γ, τ_1, τ_2, and τ_{tot}, one can calculate the first term in (13) and subtract it from $\phi_{out}(t)$ to extract $\Delta\phi_r$ and determine the phase slope. In this paper; however, $\Delta\phi_r$ is extracted from (13) through a calibration procedure (presented in Section IV) which also improves the accuracy of the proposed method.

III. ERROR ANALYSIS

In this part, the accuracy of the approximation in (8) is verified, and it is shown that the systematic error caused by approximating $H_s(f_I)$ with $H_r(f_I)$ is negligible under certain conditions.

Substituting $e^{j\pi\gamma\tau^2}$ by its Taylor series expansion and using the properties of Fourier transform, $H_s(f)$ is given by:

$$\begin{aligned} H_s(f) &= \mathcal{F}\left(h(\tau)\, e^{j\pi\gamma\tau^2}\right) = \mathcal{F}\left(\sum_{n=0}^{\infty} h(\tau)\frac{\left(j\pi\gamma\tau^2\right)^n}{n!}\right) \\ &= \sum_{n=0}^{\infty} \frac{1}{n!}\left(\frac{-j\gamma}{4\pi}\right)^n H_r^{(2n)}(f), \end{aligned} \tag{14}$$

where $H_r^{(2n)}$ represents the $2n$-th derivative of $H_r(f)$ with respect to f. The first term in $H_s(f)$, corresponding to $n = 0$, is equal to $H_r(f)$, while the summation of the other terms determines the systematic error in the proposed method.

For a second order resonator, $H_r(f)$ is given by:

$$H_r(f) = \frac{j\left(\frac{f_r}{Q}\right)f}{-f^2 + j\left(\frac{f_r}{Q}\right)f + f_r^2}. \tag{15}$$

For $Q \gg 1$ (thereby $\sqrt{4Q^2-1} \cong 2Q$) and at RF and microwave frequencies, $H_r(f)$ can be accurately approximated by a simple pole as:

$$H_r(f) = \frac{-j\frac{1}{4}f_r\,(j+2Q)}{Q^2\left(f - f_r - \frac{j}{2}\left(\frac{f_r}{Q}\right)\right)}. \tag{16}$$

Substituting (16) into (14) results in:

$$H_s(f) = \left(\frac{f_r}{2jQ}\right)\left(\frac{1}{\sqrt{\frac{j\gamma}{4\pi}}}\right)\sum_{n=0}^{+\infty} \underbrace{\frac{(2n)!\,(-1)^n}{n!\left(\frac{\Delta f - \frac{j}{2}\left(\frac{f_r}{Q}\right)}{\sqrt{\frac{j\gamma}{4\pi}}}\right)^{2n+1}}}_{q}, \tag{17}$$

where $\Delta f = f - f_r$. The summation in (17) cannot be, in general, represented in a closed form. For a small absolute value of q, a large number of terms are required for the convergence of the summation with a negligible trunctioan error. However, for a large absolute value of q, (17) is equal to a Faddeeva function which can be approximated by different rational functions depending on the desired accuracy [17]. Using a closed form approximation (a rational function) for $H_s(f)$ in (17) allows for specifying its phase slope and therewith the detected values for f_r and Q. One can compare the results with the actual values of f_r and Q (obtained from $H_r(f)$) to quantify the systematic error in the proposed measurement tachnique. Here, though, the described error is qualitatively analyzed (based on (17)) and then accurately evaluated using MATLAB simulations described later in this section (rather than approximating the summation in (17)).

Phase slope of $H_s(f)$ is given by:

$$\frac{d\phi}{df} = \frac{d\phi}{d(\Delta f)} = Im\left(\frac{\frac{\partial H_s}{\partial(\Delta f)}}{H_s}\right), \tag{18}$$

where $Im(.)$ denotes the imaginary part of (.). The detected resonant frequency ($f_{r,d}$) is the frequency of maximum phase slope where the derivative of (18) with respect to f (or equivalently Δf) is equal to zero. The corresponding Δf ($\Delta f_d = f_{r,d} - f_r$) represents the error in estimated resonant frequency and is only a function of γ and f_r/Q (according to (17) and (18)). Using the relation between the maximum phase slope and Q-factor in (1), the detected Q-factor (Q_d) is equal to:

$$\begin{aligned} Q_d &= \frac{f_{r,d}}{2}\left(-\frac{d\phi(f)}{df}\right)\Big|_{f_{r,d}} \\ &= \frac{f_r\left(1+\frac{\Delta f_d}{f_r}\right)}{2}\left(-\frac{d\phi(f)}{df}\right)\Big|_{f_{r,d}}. \end{aligned} \tag{19}$$

For $\Delta f_d / f_r \ll 1$, Q_d is given by:

$$Q_d \cong \frac{f_r}{2}\left(-\frac{d\phi(f)}{df}\right)\Big|_{f_{r,d}}. \tag{20}$$

The relative error in estimated Q-factor is:

$$\left|\frac{Q_d - Q}{Q}\right| = \left|\frac{Q_d}{Q} - 1\right| \cong \left|\frac{f_r}{2Q}\left(-\frac{d\phi(f)}{df}\right)\Big|_{f_{r,d}} - 1\right|. \tag{21}$$

The value of phase slope at $f_{r,d}$ (where $\Delta f = \Delta f_d$) is a function of f_r/Q and γ, and consequently, the relative error in detected Q is also a function of f_r/Q and γ.

Here, the discussed errors (in characterized resonant frequency and Q) are assessed using MATLAB simulations. In these simulations, the following steps are taken:

I. Fourier transform of the chirp signal, $S_i(f)$, is calculated and multiplied by $H_r(f)$.
II. The inverse Fourier transform of $S_i(f) \times H_r(f)$ is evaluated to obtain $s_r(t)$.
III. $s_r(t)$ is divided by $s(t)$ to calculate $H_s(f)$ following (7).
IV. Phase slope of $H_s(f)$ is derived and compared with that of $H_r(f)$.

The simulated results in Fig. 2 show the phase and phase slope of $H_s(f)$, evaluated within the steps I–IV, for two second order resonators with $f_r = 1600$ MHz and two different values of Q (or equivalently two different values of f_r/Q). The results are obtained for different values of γ and are shown versus f_I (using the linear time-frequency relationship of the chirp signal). The chirp instantaneous frequency is varied from 1590 MHz to 1610 MHz, and as can be observed in Fig. 2(a), in all cases, the transient response is vanished before f_I approaches 1592 MHz. Thus, there is no transient variation in the vicinity of $f_r = 1600$ MHz. In Fig. 2(b), the characterized phase slope is derived from $H_s(f)$, while the actual phase slope is calculated from $H_r(f)$ given in (15), and they are shown within 1599–1601 MHz for a better clarity. According to Fig. 2(b), the detected values for maximum phase slope (determining Q_d) and its corresponding frequency ($f_{r,d}$) deviate from their actual values as γ increases or f_r/Q decreases. Figure 3 shows the errors in detected resonant frequency and Q-factor versus γ and f_r/Q for several second-order resonators with different values of f_r. The error in estimated resonant frequency ($\Delta f_d = f_{r,d} - f_r$) increases as γ increases or f_r/Q decreases, as shown in Fig. 3(a). This error is relatively negligible for the indicated range of parameters. The relative error in estimated resonant frequency ($= \Delta f_d/f_r$) is inversely proportional to f_r, as shown in Fig. 3(b). According to Fig. 3(c), the relative error in detected Q also increases as γ increases or f_r/Q decreases. The results obtained for different values of f_r overlay in Fig. 3(a) and Fig. 3(c), which shows that Δf_d and the relative error in detected Q do not vary with f_r so far as f_r/Q is constant. Based on the results in Fig. 3, to characterize the Q-factor and resonant frequency of high-Q resonators accurately, γ should be set to small values. It means that there is a trade-off between the speed and accuracy of the proposed measurement technique when it is used to characterize high-Q resonators.

IV. CALIBRATION PROCESS

Here, a calibration process for an accurate measurement of the phase slope of a resonator under test is presented. This procedure allows for partially accounting for the discussed systematic error and thus improves the accuracy of the described measurement method.

In this calibration process, the resonator is first replaced by a small transmission line, and the output phase is measured for the substitute transmission line. This phase is equal to:

$$\begin{aligned} &\phi_{out,cal}(t) \\ &= (-2\pi(f_0 + \gamma(t - \tau_{tot})) + \pi\gamma(\tau_1 + \tau_2))\Delta\tau \\ &\quad + \underbrace{(\phi_{TL}(f_I(t - \tau_{tot} - \tau_2)) - \phi_{TL}(f_I(t - \tau_{tot} - \tau_1)))}_{\Delta\phi_{TL}}, \end{aligned} \tag{22}$$

where $\phi_{TL}(f)$ denotes the insertion phase of the substitute line at the frequency of f. The last term in (22), $\Delta\phi_{TL}$, is a function

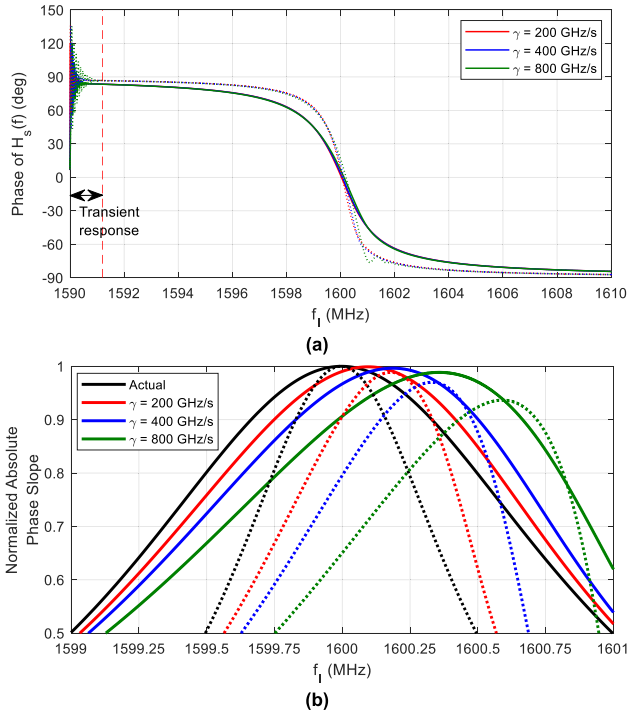

FIGURE 2. Simulation results for (a) phase of $H_s(f)$ and (b) phase slope of $H_s(f)$ for two second order resonators with $f_r = 1600$ MHz and two different values of f_r/Q (solid line: $f_r/Q = 2$ MHz and dotted line: $f_r/Q = 1$ MHz). Results are obtained for different chirp rates. The chirp instantaneous frequency, $f_I(t)$, is varied from 1590 MHz to 1610 MHz, and the transient response is vanished before $f_I(t)$ approaches 1592 MHz as shown in (a). There is no transient variation within the frequency range shown in (b).

of the length and wave propagation velocity of the substitute line and remains constant as f_I varies in time.

Subsequently, $\phi_{out}(t)$ is measured for the resonator under test. Based on (13) and taking the systematic error (caused by approximating $H_s(f_I)$ with $H_r(f_I)$ in (8)) into account, $\phi_{out}(t)$ is given by:

$$\begin{aligned}\phi_{out}(t) = {} & (-2\pi(f_0 + \gamma(t - \tau_{tot})) + \pi\gamma(\tau_1 + \tau_2))\Delta\tau \\ & + \Delta\phi_r(t) \\ & + \underbrace{(\phi_e(f_I(t - \tau_{tot} - \tau_2)) - \phi_e(f_I(t - \tau_{tot} - \tau_1)))}_{\Delta\phi_e(t)},\end{aligned} \tag{23}$$

where $\phi_e(f)$ represents the phase error at the frequency of f.

The difference between $\phi_{out}(t)$ and $\phi_{out,cal}(t)$ is given by:

$$\phi_{out}(t) - \phi_{out,cal}(t) = \Delta\phi_r(t) + \Delta\phi_e(t) - \Delta\phi_{TL}, \tag{24}$$

where $\Delta\phi_r(t)$ and $\Delta\phi_e(t)$ are equal to (25) and (26), respectively:

$$\Delta\phi_r(t) = \frac{d\phi_r(f)}{df}\Delta f = \frac{d\phi_r(f)}{df}\gamma\Delta\tau \tag{25}$$

$$\Delta\phi_e(t) = \frac{d\phi_e(f)}{df}\Delta f = \frac{d\phi_e(f)}{df}\gamma\Delta\tau. \tag{26}$$

The maximum value of $\phi_{out}(t) - \phi_{out,cal}(t)$ in (24) occurs at $t = t_r$ (corresponding to $f_I = f_{r,d}$), and based on (25) and

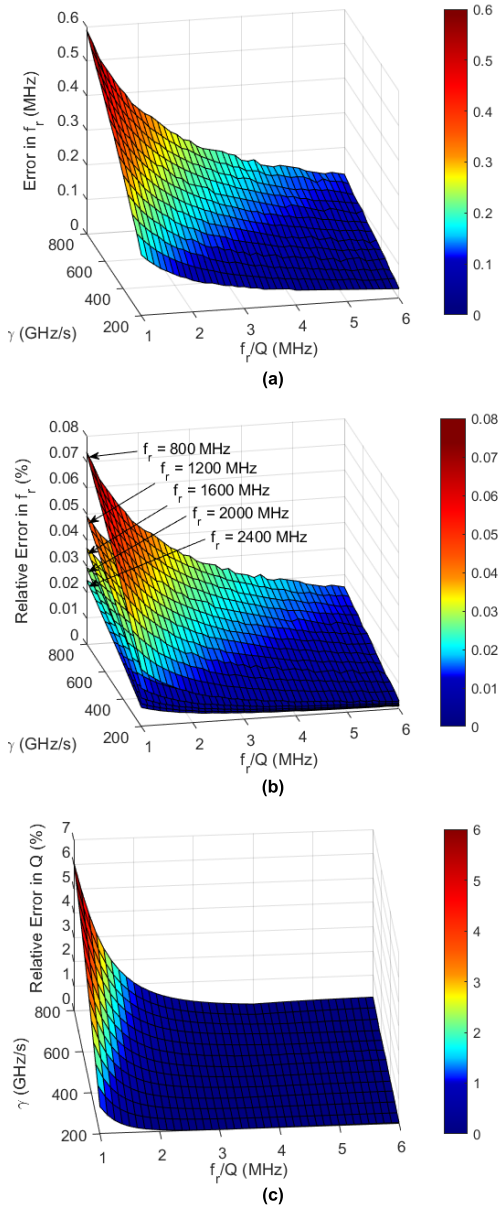

FIGURE 3. Simulated results for (a) error in detected resonant frequency ($\Delta f_d = f_{r,d} - f_r$), (b) relative error in estimated resonant frequency ($= \Delta f_d/f_r$), and (c) relative error in detected Q-factor for several second order resonators with different resonant frequencies. The results obtained for different values of f_r overlay in (a) and (c), showing that Δf_d and the relative error in detected Q do not vary with f_r so far as f_r/Q is constant.

(26), it is equal to:

$$\begin{aligned}&\max\left(\phi_{out}(t) - \phi_{out,cal}(t)\right) \\ &= \phi_{out}(t_r) - \phi_{out,cal}(t_r) \\ &= \left(\frac{d\phi_r(f)}{df} + \frac{d\phi_e(f)}{df}\right)\Big|_{f_{r,d}} \times \gamma\Delta\tau - \Delta\phi_{TL}.\end{aligned} \tag{27}$$

Considering that at $f_{r,d}$, Δf ($= \Delta f_d$) is a function of γ and f_r/Q (Section III), $d\phi_r(f)/df|_{f_{r,d}}$ and $d\phi_e(f)/df|_{f_{r,d}}$ (determined by the first term and the summation of the other terms in $H_s(f)$, respectively) are also functions of γ and f_r/Q.

Therefore, $\phi_{out}(t_r) - \phi_{out,cal}(t_r)$ in (27) is also a function of γ and f_r/Q (or equivalenty Q/f_r).

The resonator's phase slope at $f_{r,d}$ can be written as:

$$\left(-\frac{d\phi_r(f)}{df}\right)\Big|_{f_{r,d}} = \left(-\frac{d\phi_r(f)}{df}\right)\Big|_{f_r} + \epsilon_s, \qquad (28)$$

where ϵ_s represents the difference between the resonator's phase slope at $f_{r,d}$ and f_r. Considering that the resonator's phase slope at f_r follows (1) and $d\phi_r(f)/df|_{f_r,d}$ is a function of γ and f_r/Q, it can be deduced that ϵ_s is also a function of γ and f_r/Q (or equivalenty Q/f_r). Therefore, using (1), (28) can be written as:

$$\left(-\frac{d\phi_r(f)}{df}\right)\Big|_{f_{r,d}} = 2\left(\frac{Q}{f_r}\right) + \epsilon_s\left(\gamma, \frac{Q}{f_r}\right). \qquad (29)$$

Substituting (29) into (27) and replacing $d\phi_e(f)/df|_{f_r,d}$ by a general function (ϵ_p) of γ and Q/f_r results in:

$$\phi_{out}(t_r) - \phi_{out,cal}(t_r) = \gamma\Delta\tau\left(2\left(\frac{Q}{f_r}\right) + \epsilon\left(\gamma, \frac{Q}{f_r}\right)\right) - \Delta\phi_{TL}, \qquad (30)$$

where $\epsilon = \epsilon_s + \epsilon_p$. Taking (30) into account, the resonator's Q-factor and resonant frequency can be characterized following the procedure below.

I. $\phi_{out,cal}(t)$ is measured over the chirp sweep time.
II. $\phi_{out}(t)$ is measured for several resonators with known Q/f_r, and for each resonator, $\phi_{out}(t) - \phi_{out,cal}(t)$ is evaluated over the chirp sweep time.
III. The maximum value of $\phi_{out}(t) - \phi_{out,cal}(t)$, which occurs at $t = t_r$, is determined for each resonator.
IV. The values of $\phi_{out}(t_r) - \phi_{out,cal}(t_r)$ obtained for several known resonators are plotted versus actual Q/f_r. According to (30), the results should ideally ($\epsilon(\gamma, Q/f_r) = 0$) lie on a line; however, they are slightly off due to the discussed systematic error. One can partially account for this error by specifying the line of best fit to the data points and use the equation of this line to calculate the Q-factor of resonators under test (through VI and VII).
V. To characterize an unknown resonator, $\phi_{out}(t)$ is measured for the resonator under test. Subsequently, $\phi_{out}(t) - \phi_{out,cal}(t)$ is evaluated for the resonator over the chirp sweep time, and the time at which it obtains its maximum value is ascertained. The instantaneous frequency corresponding to this time is the detected resonant frequency ($f_{r,d}$) for the resonator under test.
VI. The maximum value of $\phi_{out}(t) - \phi_{out,cal}(t)$, which is equal to $\phi_{out}(t_r) - \phi_{out,cal}(t_r)$, is evaluated for the resonator under test. Subsequently, the equation of the best fitted line (obtained in IV) is used to determine the resonator's Q/f_r from $\phi_{out}(t_r) - \phi_{out,cal}(t_r)$.
VII. Finally, the resonator's Q-factor can be calculated by multiplying Q/f_r (estimated in VI) by $f_{r,d}$ (specified in V).

Figure 4(a) shows the simulated $\phi_{out}(t) - \phi_{out,cal}(t)$ versus $f_I(t)$ for several resonators with an actual f_r of 1600 MHz and different Q-factors. The solid and dashed lines show the results for the known resonators (used for calibration) and the resonators under test, respectively. In this simulation, γ is set to 750 GHz/s, and the electrical length of the substitute transmission line (used for calibration) is 9.6° at 1600 MHz. According to the results, the characterized resonant frequency ($f_{r,d}$), which is the frequency of maximum value for $\phi_{out} - \phi_{out,cal}$, is off by less than 0.5 MHz, resulting in a less than 0.04% error. Figure 4(b) shows the relation between $\phi_{out}(t_r) - \phi_{out,cal}(t_r)$ and the actual Q/f_r for the resonators given in Fig. 4(a). It also shows the line of best fit to the

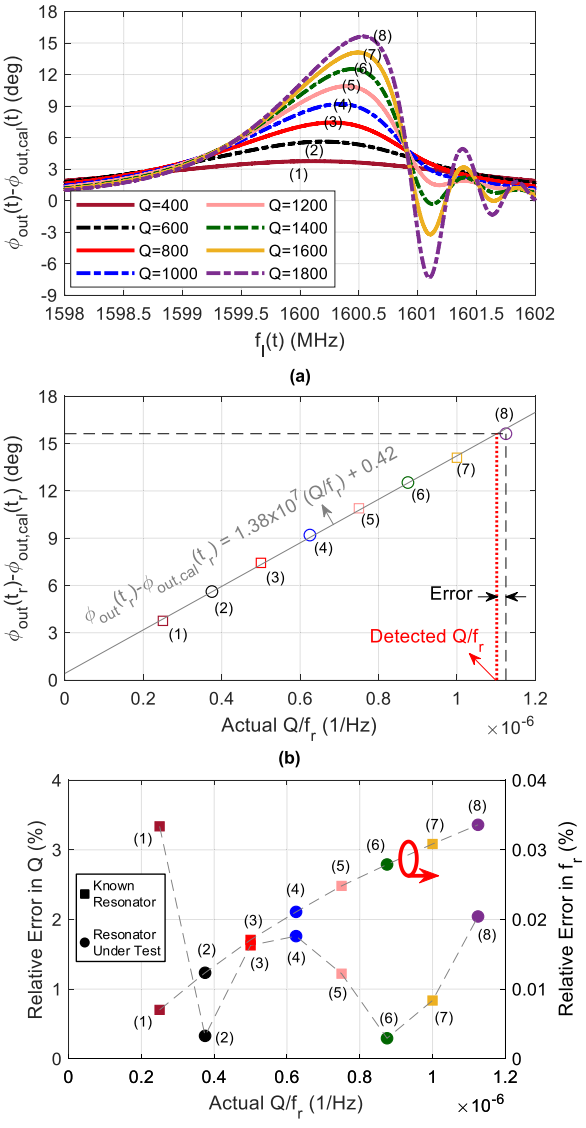

FIGURE 4. (a) Simulation results for $\phi_{out}(t) - \phi_{out,cal}(t)$ versus $f_I(t)$ for several resonators with f_r = 1600 MHz and different Q-factors. Solid and dashed lines are for known resonators (used for calibration purposes) and the resonators under test, respectively. (b) Simulated $\phi_{out}(t_r) - \phi_{out,cal}(t_r)$ versus actual Q/f_r for the resonators given in (a). Solid line is the line of best fit to the data points indicated by squares (obtained for known resonators). (c) Relative error in estimated Q and resonant frequency versus actual Q/f_r for the resonators given in (a). In figures (a)–(c), the data points or traces with the same color and number are related to the same simulation.

data points obtained for known resonators. Using this line to calculate Q-factor of the resonators under test from their simulated $\phi_{out}\,(t_r) - \phi_{out,cal}\,(t_r)$ results in a less than 4% error in estimated Q, as shown in Fig. 4(c).

V. MEASUREMENT SYSTEM

The setup shown in Fig. 5 is used to implement the described measurement approach. A linear chirp generator operating within 1200–1968 MHz (L-band) is designed and fabricated for measurement purposes. In this chirp generator, shown in Fig. 6, a low phase noise direct digital synthesizer (DDS) is used to generate a linear chirp with the frequency range of 50-82 MHz. This low-frequency chirp signal is input to a PLL, and its frequency is multiplied by a factor of 24 using the PLL circuit. The utilized DDS (Analog Devices AD9911) is controlled by an enable signal which commands the block to start sweeping the low-frequency chirp. The start time of this sweep is used as a reference for mapping time to the chirp instantaneous frequency. The utilized PLL consists of a wideband VCO (Mini Circuits ROS-2420), an active loop filter, and a wide band phase frequency detector (Analog Devices HMC439), allowing for a fast locking time. The PLL's output signal is amplified by 13 dB (using a HMC374 amplifier) and injected into the resonator under test which is an L-band cavity resonator partially filled with wet sand. The resonator's output signal is amplified by 25 dB (using a Mini Circuits MNA-6A+) and subsequently divided into two parts using a 3-dB divider. The two equal signals coming out of the divider are delayed by a short and a longer transmission line. The delay difference between these lines (coaxial cables) is 174 ns, resulting in a frequency difference of 130.5 kHz between their output signals. The signals coming out of the short and the longer transmission lines are connected to the LO and RF ports of an I/Q mixer (SKY 7300911) used as a phase detector, respectively. The mixer's output signals are sampled with a rate of 25 MSamples/s and converted to digital signals using 16-bit analog to digital converters (A/D).

VI. MEASUREMENT RESULTS

Measurements are performed within two different frequency bands, 1250–1450 MHz and 1500–1700 MHz, and the start and stop frequencies of the chirp signal are properly set for each band. The frequency and time steps are also set to 6 kHz and 8 ns, resulting in a chirp rate of 750 GHz/s. Hence, the chirp sweep time is less than 270 μs, allowing for a fast measurement.

The resonant frequency of the cavity resonator used for measurement purposes is nearly 1620 MHz. For measurements at the upper frequency band, the cavity resonator was partially filled with wet sand, while for measurements at the lower band, a metallic object was also inserted into the cavity resonator (to decrease its resonant frequency). Resonant frequency and Q-factor of the partially-filled cavity resonator depend on the volume and moisture content of the sand inside it. Several measurements are performed with

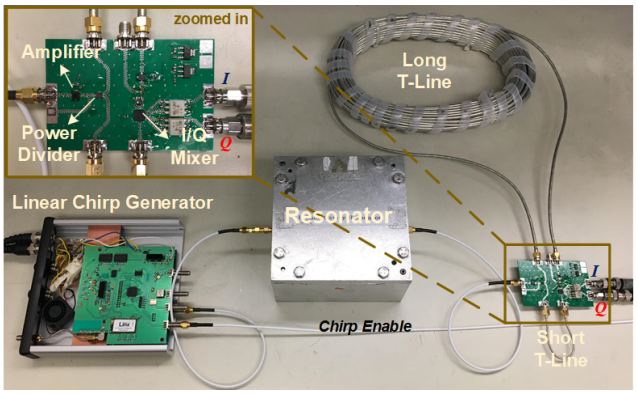

FIGURE 5. Measurement setup [14].

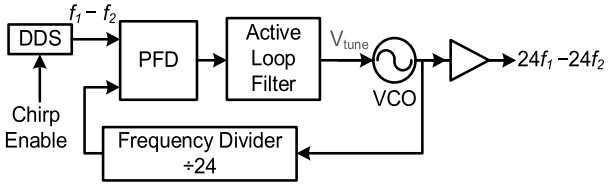

FIGURE 6. Block diagram of the chirp generator.

different samples of sand (with different volume and moisture content), and the measured results for $\phi_{out}(t) - \phi_{out,cal}(t)$ versus $f_I(t)$ are shown in Fig. 7(a). The characterized resonant frequency ($f_{r,d}$), which is the frequency of maximum $\phi_{out}(t) - \phi_{out,cal}(t)$, is shown for each resonator. The actual resonant frequencies (f_r) of the utilized resonators are also measured, using a VNA, and included in Fig. 7(a). Based on the results, $f_{r,d}$ is nearly equal to f_r for any characterized resonator. Figure. 7(b) shows $\phi_{out}(t_r) - \phi_{out,cal}(t_r)$, which equals the maximum value of $\phi_{out}(t) - \phi_{out,cal}(t)$, versus actual Q/f_r (measured by VNA) for the resonators given in Fig. 7(a). The data points obtained for known resonators (used for calibration) are shown by squares, while the results obtained for unknown resonators are indicated by circles. The line of best fit to the data points obtained for known resonators is also shown. This line is used to calculate Q-factor of the unknown resonators from their measured values of $\phi_{out}\,(t_r) - \phi_{out,cal}\,(t_r)$. The relative error in estimated Q-factor (specified by comparing the measured results with the actual values obtained from a VNA) is less than 4%, as shown in Fig. 7(c). The relative error in detected resonant frequency is also shown in Fig. 7(d). The results verify that the proposed measurement technique estimates resonant frequency with a negligible error ($< 0.6\%$).

The best fitted lines in simulations and measurements are not the same (comparing Fig. 4(b) with Fig. 7(b)). The main reason is that $\gamma\Delta\tau$, which can considerably change the slope and y-intercept point of the best fitted line (according to (30)), has a large value in the implemented system. This results in a nontrivial difference in slope and y-intercept points of the best fitted lines in simulations and measurements for even minimal difference in their $\epsilon\left(\gamma, Q/f_r\right)$ (that can occur

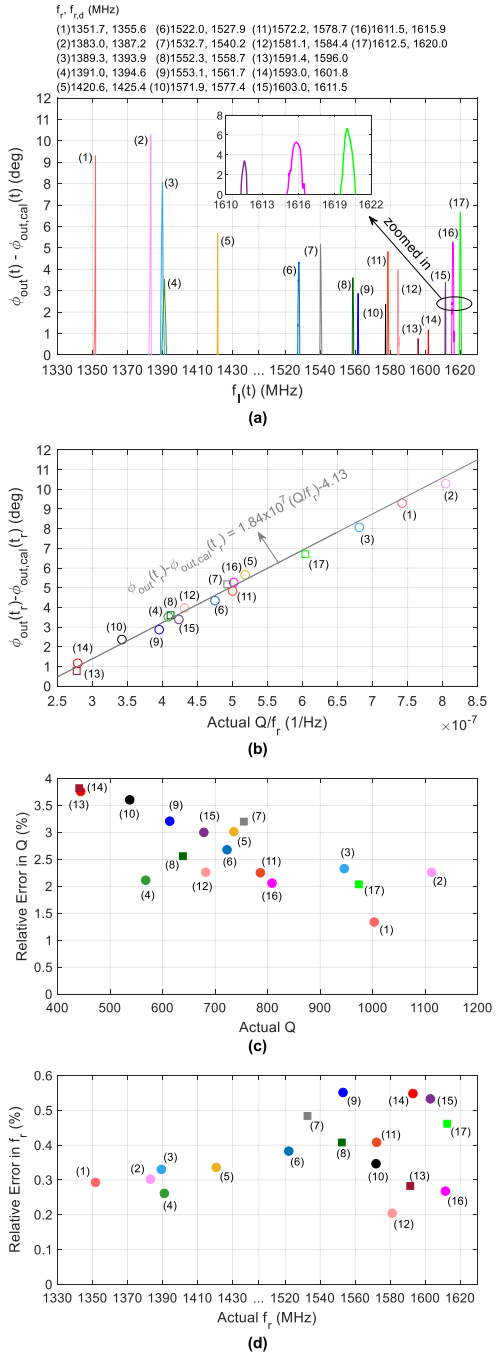

FIGURE 7. **(a) Measured $\phi_{out}(t)-\phi_{out,cal}(t)$ versus $f_I(t)$ for several different resonators. (b) Maximum values of $\phi_{out}(t)-\phi_{out,cal}(t)$ obtained from the results in (a) versus actual Q/f_r. Solid line is the best fitted line to the data points indicated by squares (obtained for known resonators). Relative error in estimated (c) Q-factor and (d) resonant frequency of the resonators given in (a). In figures (a)–(d), the data points or traces with the same color and number are related to the same measurement.**

due to the measurement non-idealities). However, it does not impact the system functionality or accuracy since for a given measurement setup, the line of best fit substantially accounts for the existing errors and non-idealities. In both simulation and measurement results, relative error in estimated Q is less than 4%. The relative error in measured resonant frequency is larger than the error in simulation results mainly due to the random delays in the circuit generating Chirp Enable signal and in A/D start time (after receiving the Chirp Enable signal). Such delays result in an error in consideration of the start time and so an error in the detected resonant frequency (obtained from the linear time-frequency relationship of the chirp signal). This error can be reduced using faster control units (e.g. fast microcontrollers) and/or an A/D with a higher maximum sampling rate.

VII. CONCLUSION

A simple, fast, and yet accurate time-domain technique for resonant frequency and Q-factor measurements of second-order resonators is presented. The applications of the presented method include but are not limited to dielectric measurements in remote sensing, geology, and sensors in industry. In this approach, phase slope of a resonator is measured and used to calculate its resonant frequency and Q-factor. A linear slow-rate chirp signal is generated and passed through the resonator under test. The output signal of the resonator is divided into two equal parts which are delayed by two different amounts. The phase difference between the delayed signals is used to determine the resonator's phase slope. Performance of the described method in characterizing both low and high-Q resonators is evaluated through simulations and measurements. It is shown that there is a trade-off between the speed and accuracy of the described method to characterize high-Q resonators. A calibration method has been presented to enhance the accuracy of the proposed method in fast measurements of high-Q resonators. Based on the results, the presented technique can measure the resonant frequency and Q-factor of resonators with less than 0.6% and 4% error, respectively.

REFERENCES

[1] J. R. Kendra, F. T. Ulaby, and K. Sarabandi, "Snow probe for *in situ* determination of wetness and density," *IEEE Trans. Geosci. Remote Sens.*, vol. 32, no. 6, pp. 1152–1159, Nov. 1994.

[2] K. Sarabandi and E. S. Li, "Microstrip ring resonator for soil moisture measurements," *IEEE Trans. Geosci. Remote Sens.*, vol. 35, no. 5, pp. 1223–1231, Sep. 1997.

[3] C.-S. Lee and C.-L. Yang, "Complementary split-ring resonators for measuring dielectric constants and loss tangents," *IEEE Microw. Wireless Compon. Lett.*, vol. 24, no. 8, pp. 563–565, Aug. 2014.

[4] M. S. Boybay and O. M. Ramahi, "Material characterization using complementary split-ring resonators," *IEEE Trans. Instrum. Meas.*, vol. 61, no. 11, pp. 3039–3046, Nov. 2012.

[5] M. Gil, P. Velez, F. Aznar-Ballesta, J. Muñoz-Enano, and F. Martín, "Differential sensor based on electroinductive wave transmission lines for dielectric constant measurements and defect detection," *IEEE Trans. Antennas Propag.*, vol. 68, no. 3, pp. 1876–1886, Mar. 2020.

[6] M. H. Zarifi, A. Sohrabi, P. M. Shaibani, M. Daneshmand, and T. Thundat, "Detection of volatile organic compounds using microwave sensors," *IEEE Sensors J.*, vol. 15, no. 1, pp. 248–254, Jan. 2015.

[7] B. Camli, H. Torun, G. Dundar, and A. D. Yalcinkaya, "Reference-incorporating microwave resonator-based sensors for biological sensing applications," *Proceedings*, vol. 1, no. 4, p. 542, Aug. 2017.

[8] J. M. Elzerman, R. Hanson, L. H. Willems van Beveren, B. Witkamp, L. M. K. Vandersypen, and L. P. Kouwenhoven, "Single-shot read-out of an individual electron spin in a quantum dot," *Nature*, vol. 430, no. 6998, pp. 431–435, Jul. 2004.

[9] D. J. Reilly, C. M. Marcus, M. P. Hanson, and A. C. Gossard, "Fast single-charge sensing with a RF quantum point contact," *Appl. Phys. Lett.*, vol. 91, no. 16, Oct. 2007, Art. no. 162101.
[10] J. Mata-Contreras, C. Herrojo, and F. Martín, "Application of split ring resonator (SRR) loaded transmission lines to the design of angular displacement and velocity sensors for space applications," *IEEE Trans. Microw. Theory Techn.*, vol. 65, no. 11, pp. 4450–4460, Nov. 2017.
[11] F. Martín, P. Vélez, and M. Gil, "Microwave sensors based on resonant elements," *Sensors*, vol. 20, no. 12, p. 3375, Jun. 2020.
[12] K. G. Ong, C. A. Grimes, C. L. Robbins, and R. S. Singh, "Design and application of a wireless, passive, resonant-circuit environmental monitoring sensor," *Sens. Actuators A, Phys.*, vol. 93, no. 1, pp. 33–43, Aug. 2001.
[13] M. Zhang and N. Llaser, "Exploiting time-domain approach for extremely high *Q*-factor measurement," *IEEE Trans. Instrum. Meas.*, vol. 64, no. 10, pp. 2730–2737, Oct. 2015.
[14] F. Akbar, B. Yektakhah, H. Xu, and K. Sarabandi, "An accurate low-cost method for *Q*-factor and resonance frequency measurements of RF and microwave resonators," in *Proc. IEEE Int. Geosci. Remote Sens. Symp. (IGARSS)*, Waikoloa, HI, USA, Sep. 2020, pp. 1432–1435.
[15] W. G. Carrara, R. S. Goodman, and R. M. Majewski, *Spotlight Synthetic Aperture Radar*. Boston, MA, USA: Artech House, 1995.
[16] A. Ribalta, "Time-domain reconstruction algorithms for FMCW-SAR," *IEEE Geosci. Remote Sens. Lett.*, vol. 8, no. 3, pp. 396–400, May 2011.
[17] M. R Zaghloul, "Efficient multi-accuracy computations of complex functions with complex arguments," Jan. 2019, *arXiv:1806.01656*. [Online]. Available: http://arxiv.org/abs/1806.01656

FATEMEH AKBAR (Member, IEEE) received the Ph.D. degree in electrical engineering from the University of Michigan, Ann Arbor, MI, USA, in 2018.

She joined the California Institute of Technology, as a Postdoctoral Research Scholar. Her current research interests include applied EM and analog, RF, mm-wave, THz, and photonic integrated circuits and systems for applications in wireless transceivers, radars, sensors, imaging, wireless power transfer, the IoT, biomedical devices, and quantum computing.

Ms. Akbar was a recipient of the Engineering Graduate Symposium Technical Award from the College of Engineering, University of Michigan, in 2014, 2016, and 2017, and invited to MIT's EECS Rising Star Workshop, in 2018.

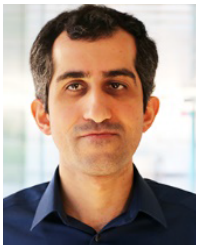

BEHZAD YEKTAKHAH (Member, IEEE) received the B.S. and M.S. degrees in electrical engineering from the University of Tehran, Tehran, Iran, in 2008 and 2011, respectively, and the Ph.D. degree in electrical engineering from the University of Michigan, Ann Arbor, MI, USA, in 2019.

He is currently a Postdoctoral Research Fellow with the University of Michigan. His research interests include through-the-wall and subsurface imaging, electromagnetic scattering, and antennas.

HAOKUI XU (Graduate Student Member, IEEE) received the B.S. degree in electrical engineering from the Beijing Institute of Technology, Beijing, in 2014, and the M.S. degree from the University of Michigan, Ann Arbor, MI, USA, in 2016, where he is currently pursuing the Ph.D. degree.

His research interests include wave scattering from terrestrial snow, thermal emission from polar ice sheet, and GNSS-R land applications.

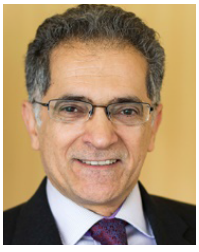

KAMAL SARABANDI (Fellow, IEEE) received the B.S. degree in electrical engineering from the Sharif University of Technology, Tehran, Iran, in 1980, the M.S. degree in electrical engineering, in 1986, and the M.S. degree in mathematics and the Ph.D. degree in electrical engineering from the University of Michigan, Ann Arbor, MI, USA, in 1989.

From 2008 to 2018, he led the Center for Microelectronics and Sensors sponsored by the Army Research Laboratory under the Micro-Autonomous Systems and Technology (MAST) Collaborative Technology Alliance (CTA) Program. He is now leading a newly established Center in Microwave Sensor Technology. He is currently the Director of the Radiation Laboratory and the Rufus S. Teesdale endowed Professor of engineering with the Department of Electrical Engineering and Computer Science, University of Michigan. He has published many book chapters and more than 280 articles in refereed journals on miniaturized and on-chip antennas, meta-materials, electromagnetic scattering, wireless channel modeling, random media modeling, microwave measurement techniques, radar calibration, inverse scattering problems, and microwave sensors. He has also had more than 650 articles and invited presentations in many national and international conferences and symposia on similar subjects. His research interests include microwave and millimeter-wave radar remote sensing, meta-materials, electromagnetic wave propagation, and antenna miniaturization.

Dr. Sarabandi served as a member for the NASA Advisory Council appointed by the NASA Administrator for two consecutive terms, from 2006 to 2010. He served as the President for the IEEE Geoscience and Remote Sensing Society (GRSS), in 2015 and 2016. He was a member of the Editorial Board of the Proceedings of the IEEE and an Associate Editor for the IEEE Transactions on Antennas and Propagation and the IEEE Sensors Journal. He is a member of the Commissions F and B of URSI. He is serving as the Chair of the USNC URSI Commission F. He was a recipient of the Henry Russel Award from the Regent of the University of Michigan, in 1997. He received a GAAC Distinguished Lecturer Award from the German Federal Ministry for Education, Science, and Technology, in 1999. He was also a recipient of the 1996 EECS Department Teaching Excellence Award. He received the IEEE GRSS Distinguished Achievement Award and the University of Michigan Faculty Recognition Award, in 2005. He was a recipient of the Best Paper Award at the 2006 Army Science Conference and the IEEE GRSS Symposium Best Paper Award, in 2008 and 2017. He was awarded a Humboldt Research Award from The Alexander von Humboldt Foundation of Germany, in 2008. He was also awarded the 2010 Distinguished Faculty Achievement Award from the University of Michigan. The IEEE Board of Directors announced him as a recipient of the 2011 IEEE Judith A. Resnik Award. He was recognized by the IEEE GRSS with its 2013 Education Award. He received the College of Engineering Research Excellence Award, in 2004, the Stephen S. Attwood Award, in 2017, and the Ted Kennedy Family Faculty Team Excellence Award from the College of Engineering at the University of Michigan, in 2018. He was recognized as one of the top 50 Graduates of the Sharif University of Technology, in 2016. He also received the NASA Group Achievement Award for his contributions to NASA SMAP Mission. In the past several years, joint articles presented by his students at a number of international symposia, such as IEEE APS 1995, 1997, 2000, 2001, 2003, 2005, 2006, and 2007; 2016 IEEE IGARSS 1999, 2002, 2007; 2011, 2014, IEEE IMS 2001, USNCURSI 2004, 2005, 2006, 2010, 2011, AMTA 2006, URSI GA 2008, 2014; and Eastern Snow Conference 2016 have received best paper awards.